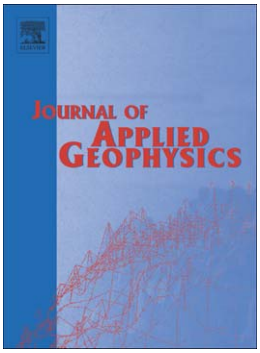


# Probabilistic estimation of reservoir properties by means of wide-angle AVA inversion and a petrophysical reformulation of the Zoeppritz equations

Mattia Aleardi, Fabio Ciabarri, Alfredo Mazzotti

PII: S0926-9851(17)30119-2
DOI: doi:10.1016/j.jappgeo.2017.10.002
Reference: APPGEO 3348

To appear in: *Journal of Applied Geophysics*

Received date: 31 January 2017
Revised date: 5 September 2017
Accepted date: 10 October 2017

Please cite this article as: Aleardi, Mattia, Ciabarri, Fabio, Mazzotti, Alfredo, Probabilistic estimation of reservoir properties by means of wide-angle AVA inversion and a petrophysical reformulation of the Zoeppritz equations, *Journal of Applied Geophysics* (2017), doi:10.1016/j.jappgeo.2017.10.002

# Probabilistic estimation of reservoir properties by means of wide-angle AVA inversion and a petrophysical reformulation of the Zoeppritz equations

**Mattia Aleardi*, Fabio Ciabarri**, Alfredo Mazzotti***

***University of Pisa, Earth Sciences Department, **Edison RD&I**

**Corresponding Author: Mattia Aleardi, mattia.aleardi@dst.unipi.it**

## Abstract

We apply a target-oriented amplitude versus angle (AVA) inversion to estimate the petrophysical properties of a gas-saturated reservoir in offshore Nile Delta. A linear empirical rock-physics model derived from well log data provides the link between the petrophysical properties (porosity, shaliness and saturation) and the P-wave, S-wave velocities and density. This rock-physics model, properly calibrated for the investigated reservoir, is used to re-parameterize the exact Zoeppritz equations. The so derived equations are the forward model engine of a linearized Bayesian AVA-petrophysical inversion that, for each data gather, inverts the AVA of the target reflections to estimate the petrophysical properties of the reservoir layer, keeping fixed the cap-rock properties. We make use of the iterative Gauss-Newton method to solve the inversion problem. For each petrophysical property of interest, we discuss the benefits introduced by wide-angle reflections in constraining the inversion and we compare the posterior probability distributions (PPDs) analytically obtained via a local linearization of the inversion with the PPDs numerically computed with a Markov Chain Monte Carlo (MCMC) method. It results that the porosity is the best resolved parameter and that wide-angle reflections effectively constrain the shaliness estimates but do not guarantee reliable saturation estimates. It also results that the local linearization returns accurate PPDs in good agreement with the MCMC estimates.

**Keywords**

Reservoir characterization; AVA inversion; probabilistic petrophysical inversion.

## 1. Introduction

The inverse problem of estimating petrophysical parameters from pre-stack seismic data is inherently non-unique and ill-conditioned; hence, an important component involves estimating the uncertainties affecting the recovered model parameters. The Bayesian formulation is the most applied method to cast the inverse problem in a statistical framework (Tarantola, 2005). From the Bayesian viewpoint, the solution to the inverse problem is the posterior probability distribution (PPD), which combines prior information about the model with information derived from the observed data. In particular, the Bayesian estimation of petrophysical rock properties from pre-stack seismic data is a very active research field that has gained broad applications in reservoir appraisal and development studies (many examples can be found in Avseth et al. 2005). Over the last decades, several probabilistic seismic-petrophysical inversion approaches have been developed with different assumptions and limitations about the modeling, the propagation of uncertainties, and the type of relations linking the rock properties to the seismic data. However, despite these differences, most of them estimate petrophysical properties in two sequential and distinct inversion steps. In the first one, a linear amplitude versus angle (AVA) inversion (Ostrander, 1984; Rutherford and Williams, 1989; Mazzotti, 1990; Mazzotti, 1991; Grion et al.,1998; Aleardi and Mazzotti 2014; Aleardi et al. 2015) is used to derive elastic parameters (such as P-wave velocity, *Vp*; shear-wave velocity, *Vs*, and, in favorable cases, density). In a second step, a petrophysical inversion converts the previously estimated elastic parameters into petrophysical properties (Mukerji et al. 2001; Contreras et al. 2005; Grana and Della Rossa, 2010). One of the drawbacks of this two-step approach concerns the error propagation from the seismic data to the final estimated petrophysical properties. If this error propagation is not done properly, the inversion can lead to errors or underestimation of the true uncertainties affecting the estimated petrophysical parameters (Li and

Zhang, 2015). In addition, as reported in Zunino et al (2014) and in Bosh (2004) in case of a non-linear inversion, the single-step approach (that directly relates the seismic response to the petrophysical properties) and the two-step approach can give similar but not equivalent results, with the two-step approach that can yield biased parameter estimations. Finally, the single-step inversion makes the sensitivity analysis of the inversion kernel more easily interpretable.

Mazzotti and Zamboni (2003) performed a single-step AVA-petrophysical inversion by using a previously calibrated empirical rock-physics model to rewrite the exact Zoepprtiz equations in terms of petrophysical properties. However, the main limits of their experiment were the very narrow angle range considered (0-26 degrees) and the very time consuming, fully non-linear, optimization procedure solved by the grid search method. Chiappa and Mazzotti (2009) developed a local linearization of the method proposed by Mazzotti and Zamboni (2003) in order to speed up the AVA inversion. However, the majority of the works concerning AVA-petrophysical inversion focus their attention on a linear inversion in a narrow-angle range (0-30 degrees, approximately). Such linear inversion is computationally fast but it assumes weak contrasts at the reflecting interface and a narrow range of incidence angles. Over the last decades, the introduction of long recording cables/streamers and new acquisition methods have enabled the recording of long-offset reflections and have increased the interests on wide-angle AVA inversion. It has been demonstrated that wide-angle reflections are helpful for better constraining the estimations of elastic parameters (Riedel et al. 2003; Zhu and McMechan, 2012; Aleardi and Tognarelli 2016), of viscoelastic properties (Riedel and Theilen, 2001) and of anisotropy parameters (Skopintseva and Alkhalifah, 2013). But to the best of our knowledge the actual benefits introduced by wide-angle reflections in constraining the reservoir properties estimated by AVA-petrophysical inversion have not been extensively discussed yet.

Independently from the approach used (single-step or two-step inversion), the core of any AVA-petrophysical inversion is the rock-physics model (RPM) that relates the elastic rock properties to the petrophysical properties. Several approaches can be used to define the RPM: they can be based

on the well-known theoretical equations (Hertz-Mindlin model, Hashin-Shtrikman bounds, Gassmann equation; see Mavko et al. 2009), or on a set of equations empirically derived from well logs or core data and specifically valid for the area under investigation (Aleardi and Ciabarri 2017).

For linear inverse problems, casted in a Bayesian framework and having Gaussian-distributed data errors and Gaussian a-priori distributions, the posterior probability distribution can be analytically obtained and it is again a Gaussian distribution. Differently, in non-linear inverse problems, even if the errors and the a-priori distribution are Gaussian distributed, the posterior distribution is no more Gaussian. Despite this substantial difference, the Bayesian inference theory provides an approach to parameter and uncertainty estimation in fully non-linear inverse problems too. In such non-linear problems, many efforts have been directed at reliably and efficiently evaluating the posterior probability distributions. For example, the error propagation could be accurately performed by means of a Markov Chain Monte Carlo (MCMC) sampling (Sambridge and Mosegaard, 2002). Such MCMC methods rely on minor assumptions on the shape of the prior and posterior probability distributions and provide accurate PPDs but at considerable computational costs. This high computational cost often prevents the application of these methods in case of inverse problems with many unknowns, or to invert large 3D seismic volumes. Examples of applications of MCMC method to AVA-petrophysical inversion can be found in Bosch et al. (2007) and Bosch et al. (2015), whereas examples of applications of MCMC algorithms to other geophysical inverse problems can be found in Sen and Stoffa (1996). It has been also proved that in case of highly non-linear inverse problems with expensive forward modeling, the combination of a stochastic, global, search method with a MCMC algorithm is able to provide accurate PPDs at affordable computational costs (Sambridge, 1999; Sajeva et al. 2016; Aleardi and Mazzotti, 2017) but this hybrid approach is not considered in this paper. In case of a non-linear inverse problem the posterior distribution can be analytically computed if the inversion is solved using a local, gradient-based, method. This approach is often preferred in solving non-linear problems because it is often very fast to converge but it results in an estimated posterior distribution that approximates the true

one. The validity of this approximation depends on the degree of nonlinearity, which is often difficult to assess a-priori.

In this work, we estimate the petrophysical properties of a clastic, gas-saturated, reservoir in offshore Nile Delta. The reservoir zone is constituted by sand channels embedded in tick shale sequences. We apply a linearized wide-angle AVA inversion to long-offset seismic data pertaining to a 3D survey over a developed field. We use a multilinear stepwise regression to derive an empirical RPM that links the elastic attributes *Vp, Vs* and density to the petrophysical properties of effective porosity ($\varphi$), water saturation (*Sw*) and wet clay volume (wet clay volume = dry clay + clay-bound water), for brevity indicated with the term shaliness (*Sh*) in the following. To take advantage of the entire range of the reflection angles from the target layer, we consider the exact, single interface, Zoeppritz equations. Following Mazzotti and Zamboni (2003) we use the empirical RPM to re-parameterize the Zoeppritz equations in terms of reservoir properties. This re-parameterization enables us to directly derive the reservoir properties from seismic data in a single-step inversion. The aim of this work is to gain a better understanding on how the inclusion of wide-angle reflections contributes to improve the resolution on the petrophysical parameters of interest. To this end, we analyze the so called residual function maps (Riedel and Theilen, 2001) and we perform a sensitivity analysis of the inversion kernel (De Nicolao et al. 1993; Aleardi, 2015). We also analyze the suitability and practical applicability of the linearized approach in deriving the final posterior probability distributions that describe the uncertainty affecting the estimated petrophysical properties. To this end, we compare the posterior distributions analytically derived by the linearized approach with those numerically computed by means of the Metropolis-Hasting (Hastings, 1970) algorithm that is a popular Markov chain Monte Carlo method.

## 2 Deriving and calibrating the empirical rock-physics model for the investigated area

Aleardi and Ciabarri (2017) compared different methods (multi-linear regression, neural networks, genetic algorithm optimization, and theoretical equations based on granular models) to derive

RPMs relating the elastic properties (P-wave, S-wave velocities and density) to the petrophysical properties of interest (effective porosity $\varphi$, water saturation *Sw* and shaliness *Sh*) in the same offshore Nile Delta reservoir object of the present study. In what follows, we make use of their empirical, multi-linear, rock-physics model, which resulted very effective both in matching the actual well log values and in predicting unknown values in blind test experiments. A stepwise multilinear regression (Draper and Smith, 1985) yields the following relations:

$$Vp\left[m/s\right] = 1732.3 + 0.542\,z + 1.647\,Sw - 28.742\,\phi - 9.056\,Sh \quad (1a)$$

$$Vs\left[m/s\right] = 1198.2 + 0.514\,z - 2.951\,Sw - 36.072\,\phi - 11.241\,Sh \quad (1b)$$

$$Density\left[Kg/m^3\right] = 2362.4 + 0.073\,z + 1.257\,Sw - 17.351\,\phi - 3.746\,Sh \quad (1c)$$

where the depth (*z*) is expressed in meters and *Sw*, $\varphi$ and *Sh* in percentage. Note that the water saturation and shaliness vary in the range from 0% to 100%, porosity from 0 up to 32-33%, whereas the depth interval (from 2400 to 2700 m, approximately) is limited to include the target sands and the encasing shales. The magnitude of the coefficients associated to the petrophysical variables in equations (1a-c) already tells us that the porosity plays the major role in determining the elastic properties, followed by the shale content and the water saturation. Therefore, in the following AVA-petrophysical inversion, we expect that the porosity and, secondarily, the shale content will be the best estimated parameters, whereas the water saturation will be less resolvable.

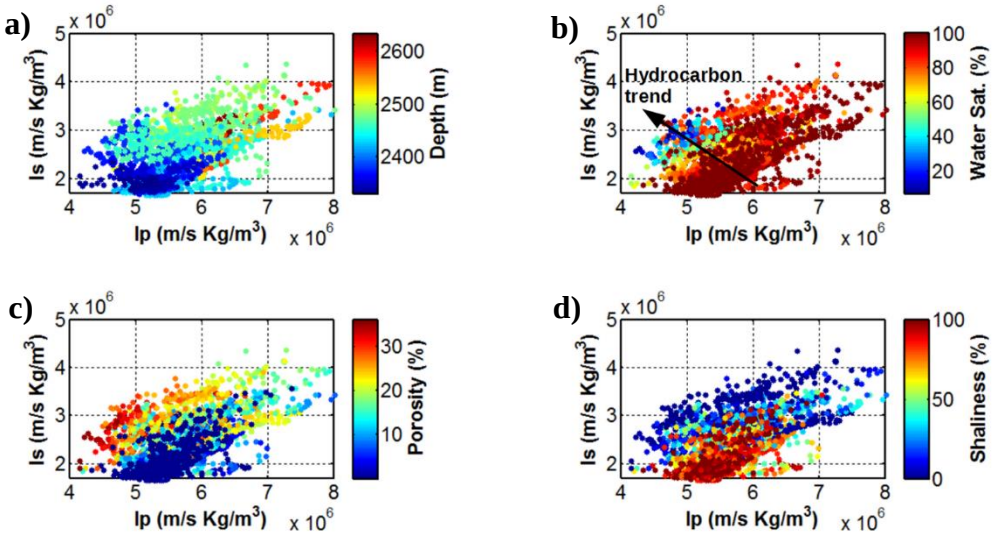


*Figure 1: a), b), c) And d) rock-physics templates derived from actual well log data and showing the Ip and Is changes with varying depth, water saturation, porosity and shaliness around the target interval, respectively. The black arrow in b) indicates the hydrocarbon trend.*

The rock-physics templates (RPTs) (Avseth et al. 2005) in Figure 1 and Figure 2 help to demonstrate the capability of equations 1a-c to reproduce the actual relations between petrophysical and elastic properties in the investigated area. Figure 1 shows the RPT derived from the actual well log data. We observe a decrease of both P-impedance (*Ip)* and S-impedance (*Is)* values with increasing porosity and with increasing shale content. In addition, the well-known hydrocarbon trend, characterized by a decrease of *Ip* and an increase of *Is* as the water saturation decrease, is evident in Figure 1b. The actual data trends in Figure 1 are well matched in the RPTs (Figure 2) derived from the empirical RPMs of equations (1a-c).

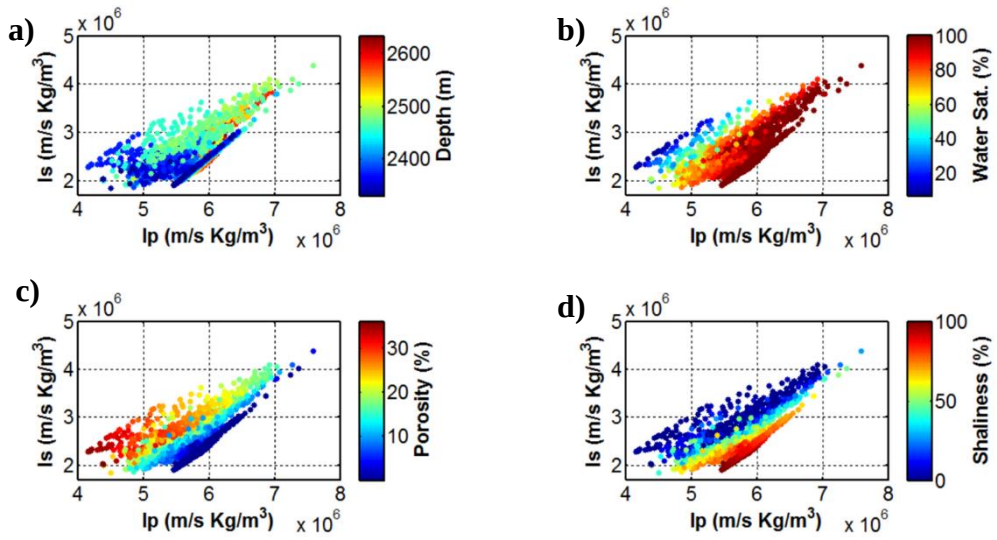


*Figure 2: a), b), c) And d) rock-physics templates predicted by the empirical linear RPM of equations (1) which show the Ip and Is changes with varying depth, water saturation, porosity and shaliness around the target interval, respectively.*

### 3 The inversion method

We use the empirical RPM of equations 1a-c to re-parameterize the exact Zoeppritz equations (Aki and Richards, 1980) in terms of petrophysical properties. The derived equation directly links the petrophysical properties (porosity, water saturation and shaliness) to the P-wave reflection coefficients and can be symbolically expressed as:

$$Rpp_{Zoeppritz-petro} = Rpp_{Zp} = f(\theta, z, \phi_{M1}, Sw_{M1}, Sh_{M1}, \phi_{M2}, Sw_{M2}, Sh_{M2}) \qquad (2)$$

where $Rpp_{Zp}$ defines our forward modeling operator that gives the P-wave reflection coefficients for an interface separating the cap-rock (*M1*) and the underlying layer (*M2*), whereas $\Theta$ and $z$ indicate the incidence angle and the target depth, respectively. By making use of equation 2 as the forward modeling in an inversion procedure allows us to directly estimate the petrophysical properties of the underlying medium (*M2*) from the observed *Rpp* response of a particular reflection, keeping fixed the petrophysical properties of the cap-rock (shale) to $\varphi$=0%, *Sh*=100% and *Sw*=100%, and setting the depth of the target zone. The inversion can be casted in a Bayesian framework, conditioned upon the normal distributions for observed data and a-priori information.

Let us consider that the $Rpp_{obs}$ is the vector containing the observed AVA response, and $m$ = [*Sw, Sh,* $\varphi$] is the vector expressing the petrophysical parameters. In a Bayesian framework, the solution of AVA-petrophysical inversion is the posterior probability distribution (PPD) of petrophysical properties conditioned upon the observed AVA response $p(m|Rpp_{obs})$. This probability distribution is the product of two terms and can be written as:

$$p(m \mid Rpp_{obs}) \propto p(Rpp_{obs} \mid m)\, p(m) \qquad (3)$$

where the first term $p(Rpp_{obs}|m)$ is the so called likelihood function that expresses the probability of observing a given AVA response ($Rpp_{obs}$) having a petrophysical model $m$. The second term $p(m)$ incorporates a-priori information about the petrophysical properties of the investigated zone that are assumed independent from the observed AVA response. If the Gaussian assumption is an acceptable approximation for all uncertainties in the problem, the likelihood function $p(Rpp_{obs}|m)$ and the a-priori distribution $p(m)$ are given by:

$$p(Rpp_{obs} \mid m) \propto \exp\left( -\frac{1}{2} (Rpp_{Zp}(m) - Rpp_{obs})^T C_D^{-1} (Rpp_{Zp}(m) - Rpp_{obs}) \right) \qquad (4a)$$

$$p(m) \propto \exp\left( -\frac{1}{2} (m - m_{prior})^T C_M^{-1} (m - m_{prior}) \right). \qquad (4b)$$

where $m_{prior}$ and $C_M$ are the a-priori mean vector and covariance matrix for reservoir properties and are determined from available borehole data. $C_D$ is the data covariance matrix and describes both the observational and theoretical errors, which in our case are the errors in the observed AVA response and the uncertainties affecting the derived RPM (both assumed Gaussian distributed with zero mean). As discussed in Tarantola (2005), the covariance matrices $C_D$ and $C_M$ incorporate the uncertainties in the data and the uncertainties related to the subsurface parameters, respectively. Tarantola (2005) also demonstrated that if all uncertainties are Gaussian distributed, the matrix $C_D$ is the sum of the covariance matrices associated with both theoretical (or in other words modeling) errors and observational errors. In our case, the modeling errors derive from the approximate formulation of the forward problem and then from the uncertainties related to the rock-physics

model used to reformulate the exact Zoeppritz equations. These considerations allow us to rewrite the $C_D$ matrix as follows:

$$C_D = C_{Rpp_{obs}} + C_{RPM} \qquad (5)$$

That is, the data covariance matrix $C_D$ is the sum of the covariance matrix of the error (noise) in the observed AVA response ($C_{Rppobs}$) and the covariance matrix associated with the uncertainties in the rock-physics model ($C_{RPM}$). Obviously, equation 5 indicates that we consider as independent the uncertainties associated to the noise in the data and to the error in the rock-physics model. See Appendix A for a detailed description on how we compute the $C_D$ matrix. To prevent overfitting the data, additional sources of errors can be added to equation 5, such as the uncertainties related to the different scale of well log data (used to derive the RPM) and seismic data (the input of the inversion). To this end, Aleardi et al. (2017) adopted an approach based on Backus averaging and Monte Carlo simulations. However, in this work only the error in the seismic data and the uncertainties in the rock-physics model are accounted for in the inversion.

From the Bayesian viewpoint, equation 3 represents the solution to the inverse problem. However, to interpret the $p(m|Rpp_{obs})$ distribution for multidimensional problems requires the computation of integral properties of the distribution. In particular, in this paper we use the posteriori marginal probability distribution for the $i$-th parameter, $p(m_i|Rpp_{obs})$, that in a general case with $M$ unknown model parameters can be written as follows:

$$p(m_i \mid Rpp_{obs}) = \int dm_1 \int dm_2 \ldots \int dm_{i-1} \int dm_{i+1} \ldots \int dm_M \, p(m \mid Rpp_{obs}) \qquad (6)$$

In the case that $p(m)$ is Gaussian distributed and $Rpp_{Zp}$ is a linear operator, both the likelihood and the posterior distribution $p(m|Rpp_{obs})$ are Gaussian. Conversely, even for Gaussian $p(m)$, the more the $Rpp_{Zp}$ diverges from a linear operator the more the likelihood diverges from the Gaussian distribution. In addition, in the case of a linear forward modeling operator the posterior distribution $p(m|Rpp_{obs})$ can be analytically computed from the likelihood and from the a-priori distribution. If the forward modeling operator is not linear the $p(m|Rpp_{obs})$ can be approximately derived through a

local linearization. In this case, the solution of the inverse problem can be found by iteratively minimizing the following error function:

$$E(m) = \| Rpp_{Zp}(m) - Rpp_{obs} \|^2_{C_D} + \| m - m_{prior} \|^2_{C_M} =$$
$$= (Rpp_{Zp}(m) - Rpp_{obs})^T C_D^{-1} (Rpp_{Zp}(m) - Rpp_{obs}) + (m - m_{prior})^T C_M^{-1} (m - m_{prior}) \quad (7)$$

where $Rpp_{Zp}(m)$ represents the predicted AVA response. This equation can be minimized through an iterative linearization of the forward problem (the $Rpp_{Zp}$ expression of equation 2) with the local, gradient-based, Gauss-Newton (GN) method that is briefly described in the following.

A local linearization can be obtained by expanding $Rpp_{Zp}(m)$ in a first order Taylor series around an arbitrary starting model $m_0$:

$$Rpp_{Zp}(m) = Rpp_{Zp}(m_0) + J(m_0)\Delta m \quad (8)$$

where $J$ is the sensitivity kernel also called Jacobian matrix:

$$J_{ij} = \frac{\partial R_{Zp}(m)_i}{\partial m_j} \quad (9)$$

The perturbation model $\Delta m_n$ at the *n-th* iteration can be obtained with the following formula:

$$\Delta m_n = -[H(m_n)]^{-1} \nabla_m E(m_n) \quad (10)$$

where $\nabla_m E(m_n)$ and $H(m_n)$ are the first and second derivatives of the error function with respect to the model parameters. They are also referred to as the gradient and the Hessian of the error function, respectively. In the framework of a statistical, Bayesian formulation, the gradient of the misfit function at the *n-th* iteration can be computed as follows (Tarantola, 2005):

$$\nabla_m E(m_n) = J_n^T C_D^{-1} (Rpp_{Zp}(m_n) - Rpp_{obs}) + C_M^{-1} (m_n - m_{prior}) \quad (11)$$

The Gauss-Newton method uses a first order approximation of the Hessian that is given by:

$$H_a(m_n) = J_n^T C_D^{-1} J_n + C_M^{-1} \quad (12)$$

where $H_a$ indicates the approximated Hessian. The previous expressions for the gradient and the approximated Hessian can be inserted into equation 10 to derive the perturbation model vector for the *n*-th iteration. To compute the Jacobian matrix, we apply a finite difference approach that

approximates the partial derivative of the predicted data ($Rpp_{pre}$) at the *n*-th iteration with respect to the *j*-th model parameter, as follows:

$$\frac{\partial Rpp^{n}_{pre}}{\partial m_j} \approx \frac{Rpp_{Zp}\left(m_n + h_j\right) - Rpp_{Zp}\left(m_n\right)}{h_j} \qquad (13)$$

where $h_j$ represents an arbitrary increment of the *j*-th model parameter.

Assuming that a linear approximation is good in the neighborhood of the best GN estimation, the posterior probability distribution can be well approximated by a Gaussian function centered at the estimated model and with posterior covariance given by:

$$C_M^{post} = C_M - C_M J^T (JC_M J^T + C_D)^{-1} JC_M \qquad (14)$$

Since the linearization may be valid only locally, the inversion should be performed different times starting from different initial models to ensure a good solution. In particular, to avoid premature convergence or trapping into local minima, we selected as final result the model resulting in the best data prediction estimated from many consecutive inversions that use different starting models, defined with uniform distribution within plausible ranges of petrophysical properties.

### 3.1 Numerical evaluation of the posterior distribution $p(m|Rpp_{obs})$

As previously introduced, in a Bayesian inversion much effort is directed at efficiently evaluating expressions such as the posterior distributions of equation 3. This distribution can be analytically evaluated in case of a linear inverse problem or in case of a non-linear problem solved by a local linearization. However, as previously mentioned the local linearization of a non-linear problem only produces an approximated estimate of such distribution. Therefore, to validate the posterior distributions analytically derived via a local linearization (see the previous section), we numerically compute (i.e. without assuming linearity) the PPD by means of the Metropolis-Hastings (M-H) algorithm. With the M-H algorithm a petrophysical model is randomly extracted from a candidate a-priori distribution (the $p(m)$ of equation 4b) and the likelihood function associated with

this model is computed. Such model is randomly perturbed and the perturbation is accepted if a random number $v$ uniformly distributed over [0 1] satisfies:

$$v \leq \frac{p(Rpp_{obs} \mid m_{pert})}{p(Rpp_{obs} \mid m_{accepted})} \qquad (15)$$

where $m_{pert}$ is the perturbed model and $m_{accepted}$ is the original, unperturbed, model. This process is repeated many times until convergence to a stable posterior distribution is attained. We compute the M-H estimate of the posterior distribution by summing the results of 10 different Markov chains, with 2000 models per chain and with a burn-in period of 1000 sampled models. We use the potential scale reduction factor to check the convergence of the M-H algorithm (Gelman et al. 2013). Once the M-H has explored the model space defined by the petrophysical properties, the marginal distributions $p(m_i|Rpp_{obs})$ can be derived with a numerical evaluation of the integral in equation 6, that is a repeated sum over the ensemble of petrophysical models sampled by the M-H algorithm.

## 4 Analyzing the 2D residual function maps

To qualitatively evaluate the influence of each petrophysical parameter in determining the AVA response of a reflecting interface and the benefits introduced by wide-angle reflections in better constraining the estimated petrophysical properties, we analyze the so called 2D residual function maps (Drufuca and Mazzotti, 1995; Riedel and Theilen, 2001) for a very simple and schematic case. Residual function maps are 1D or 2D cross-sections of residual functions plotted as a function of one or two parameters, respectively, with the other parameters kept fixed at their true, or estimated, value. Note that residual function maps give a hint on the relative sensitivity of the data to the various physical parameters but do not provide a quantitative estimation of the true uncertainties affecting the unknown parameters.

We consider a reference model with a single reflecting interface separating an overlying shale and an underlying sand (shale-sand contact). For the shale, we impose a shaliness equal to 100%, a

porosity of 0% and a total water saturation, whereas the sand has a porosity equal to 25%, a shaliness of 20% and a water saturation equal to 30%. On this model, we derive the associated AVA response by means of equation 2, then we keep fixed the petrophysical properties of the overlying shale and we vary the properties of the underlying sand layer. For each explored triad of sand petrophysical properties we compute the associated AVA response and we derive the L2 norm difference between the new AVA response and the AVA response of the reference model. We repeat this exercise for two different ranges of incidence angles:0-30 and 0-60 degrees. In this way, we can map the sensitivity of AVA response to the three petrophysical parameters and visualize the actual benefits introduced by wide-angle reflections. The 2D residual function maps computed for the narrow-angle and wide-angle cases are represented in Figure 3. Let us analyze the first case, where only the narrow-angle information is considered (Figure 3a). We observe a valley of minima, elongated along the *Sw* axis that confirms the difficulty to reliably estimate the actual value of this parameter. Differently, the shaliness and porosity seem to be better resolvable. The orientation of the valley of minima also indicates a positive correlation between the *Sh* and *Sw* parameters and a negative correlation between the shaliness and the porosity (note that this valley moves toward lower shaliness values as the porosity increases). If we increase the angle range up to 60 degrees, the valley of minima becomes narrower particularly along the porosity and shaliness axes and secondarily, along the water saturation axis. From these considerations emerge that increasing the angle range produces an increased resolution on the shaliness and the porosity parameters, but does not significantly increases the resolution on the water saturation. In other terms, increasing the angle range decreases the ambiguity in the porosity and shaliness estimates but not in the water saturation estimate. As previously discussed, the difficulty of a reliable water saturation estimation is obviously related to the minor role played by this parameter in influencing the elastic properties (see equations 1a-c).

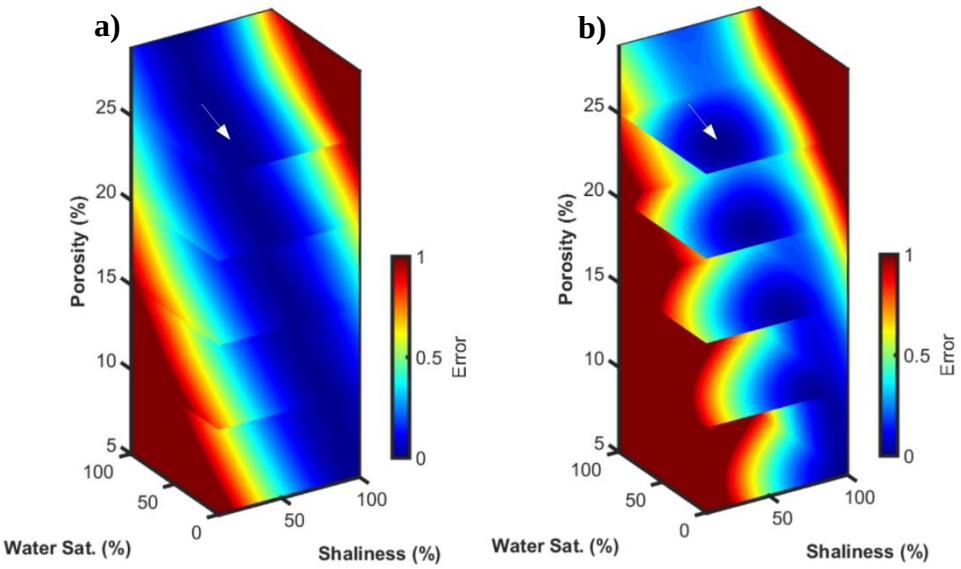


*Figure 3: a) 2D residual function maps computed for four different porosity values as the shaliness and water saturation of the underlying sand layer are varied and the shale properties are kept fixed at their original value. In this case, an angle range from 0 to 30 degrees has been considered. b) Same as in a) but considering an angle range from 0 to 60. In a) and b) the white arrows indicate the true property values. Note the same color scale in a) and b) that allows for a better comparison.*

## 5. Sensitivity analysis of the inversion kernel

To further investigate the differences between the narrow- and wide-angle inversions we make use of the SVD decomposition of the Jacobian matrix:

$$J = USV^T \qquad (16)$$

where $S$ is a diagonal matrix of singular values, $V$ is the matrix of eigenvectors in model space and $U$ contains the eigenvectors in data space. The SVD decomposition is essential in sensitivity analysis because permits to get a better understanding of the physical meaning of the Jacobian matrix. In the context of AVA inversion this decomposition splits the reflectivity *Rpp* into three orthogonal components in both data space and model space (De Nicolao et al. 1993).

The Jacobian matrix used in the following sensitivity analysis is derived from the AVA-petrophysical inversion of the simple shale-sand model introduced in the previous section. Again, the petrophysical properties of the overlying shale are kept fixed and only the sand petrophysical properties are considered as unknowns. Figure 4a, Figure 4b, and Figure 4c represent the eigenvectors in model space (*V*) associated with the first, second and third singular values of the Jacobian matrix, respectively, and represented as the maximum incidence angle considered in the inversion increases. The first eigenvector entirely points toward the direction of porosity perturbations with both the *Sw* and *Sh* components null on the entire angle range we consider.

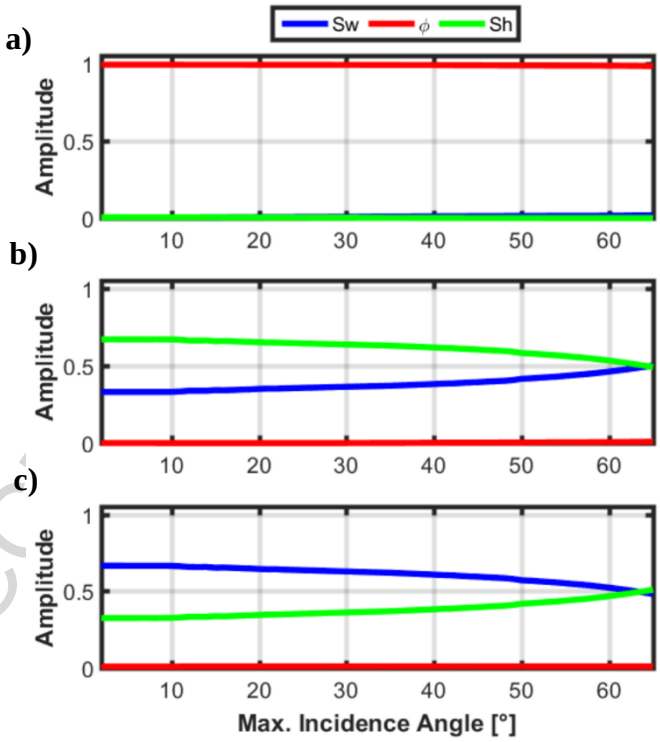


*Figure 4: Eigenvectors in model space versus the maximum observation angle. The first, second and third eigenvector are represented in a), b) and c), respectively.*

The physical meanings of the second and third eigenvectors are more difficult to interpret because they depend on combinations of shaliness and water saturation perturbations. However, it is clear that the second eigenvector is primarily influenced by the shaliness, whereas the third is mainly

associated with water saturation perturbations. These facts point out that the porosity is the best resolvable parameter followed by the shaliness that exhibits a predominant influence on the second eigenvector over the entire angle range 0-65 degrees. The water saturation only influences the third eigenvector and this proves that its estimation still remains a very ill-conditioned when a wide-angle range is used. Roughly speaking we can say that the porosity is entirely estimated from the first eigenvector, the shaliness is mainly determined from the second eigenvector, whereas the water saturation is given by the third eigenvector. In other words, porosity is the parameter that mainly influences the AVA response of a shale-sand interface over the entire angle range 0-65 degrees, followed by shaliness and water saturation.

To quantitatively evaluate the expected resolution on the petrophysical parameters for the narrow- and the wide-angle inversions, we compute the so-called model resolution matrices. In fact, although in a Bayesian inversion the a-posteriori distribution contains all the information, including the one about resolution, we can perform a sensitivity appraisal of the inverse problem through the analysis of the model resolution matrix (MRM) that can be obtained as follows:

$$MRM = C_M J^T (J C_M J^T + C_D)^{-1} J \qquad (17)$$

where $J$ refers to the Jacobian matrix computed at the convergence point. The MRM matrix expresses how the true model parameters are resolved in the inversion. Obviously, the farther the resolution matrix is from the identity matrix, the worse the resolution is (Tarantola, 2005). Figure 5 shows the MRMs computed in the case of narrow-angle (Figure 5a) and wide-angle (Figure 5b) inversions for the reference shale-sand model. Both the MRMs show that the porosity is the only parameter that can be independently and accurately estimated. The narrow-angle inversion estimates of shaliness and water saturation show low resolution and a strong interdependence. The increase of the angle range up to 60 degrees, slightly increases the porosity and water saturation resolutions and produces a significant improvement of the shaliness resolution. It is clear that the saturation parameter is poorly resolvable in both narrow-angle and wide-angle inversions, whereas the increase in the angle range is essential to better constrain the shaliness estimates and to reduce

the cross-talk between the inverted parameters. These considerations about the resolution matrices are closely linked to the conclusions drawn from the eigenvector analysis.

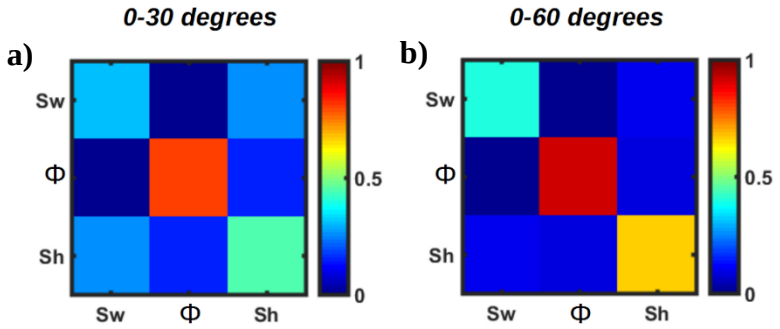


*Figure 5: a) And b) model resolution matrices computed for a narrow-angle and a wide-angle inversion, respectively. Note that the diagonal entries of the MRMs quantify the degree of independent resolvability of each petrophysical parameter, while the off-diagonal elements represent the cross-talk between model parameters in the recovered solution.*

As a final remark, before discussing the petrophysical AVA inversion of synthetic and field data, we want to point out that the conclusions drawn in this and in the previous sections are strictly related to the rock-physics model used to rewrite the exact Zoeppritz equations. In other words, different rock-physics models may lead to different conclusions.

## 6 Synthetic inversion based on actual well log data

In petrophysical AVA inversion of synthetic data, we make use of the information brought by a well that has reached the target, gas-saturated, sands. Figure 6a shows for the considered well, the litho-fluid facies classification defined on the basis of the well log data and the measured P-wave velocity (*Vp*), S-wave velocity (*Vs*) and density rescaled to the sampling interval of the available seismic reflection data (4 ms). Note the very fine shale-sand sequence and the decreases in *Vp* and in density and the increase in *Vs* occurring at the interface separating the overlying shale and the underlying gas-saturated sand. The borehole data indicate that the target sand has a porosity of 22%, a shaliness values around 20% and is approximately 30% gas-saturated (Figure 6b)**.** Resolving the

very fine layered shale-sand sequence and the limited thickness of the reservoir sands (around 10 m) that characterize this deltaic environment is a major challenge for any inversion method based on seismic data and is even more problematic in our case because of the low-resolution of the available 3D seismic data (see the discussion about the field data inversion).

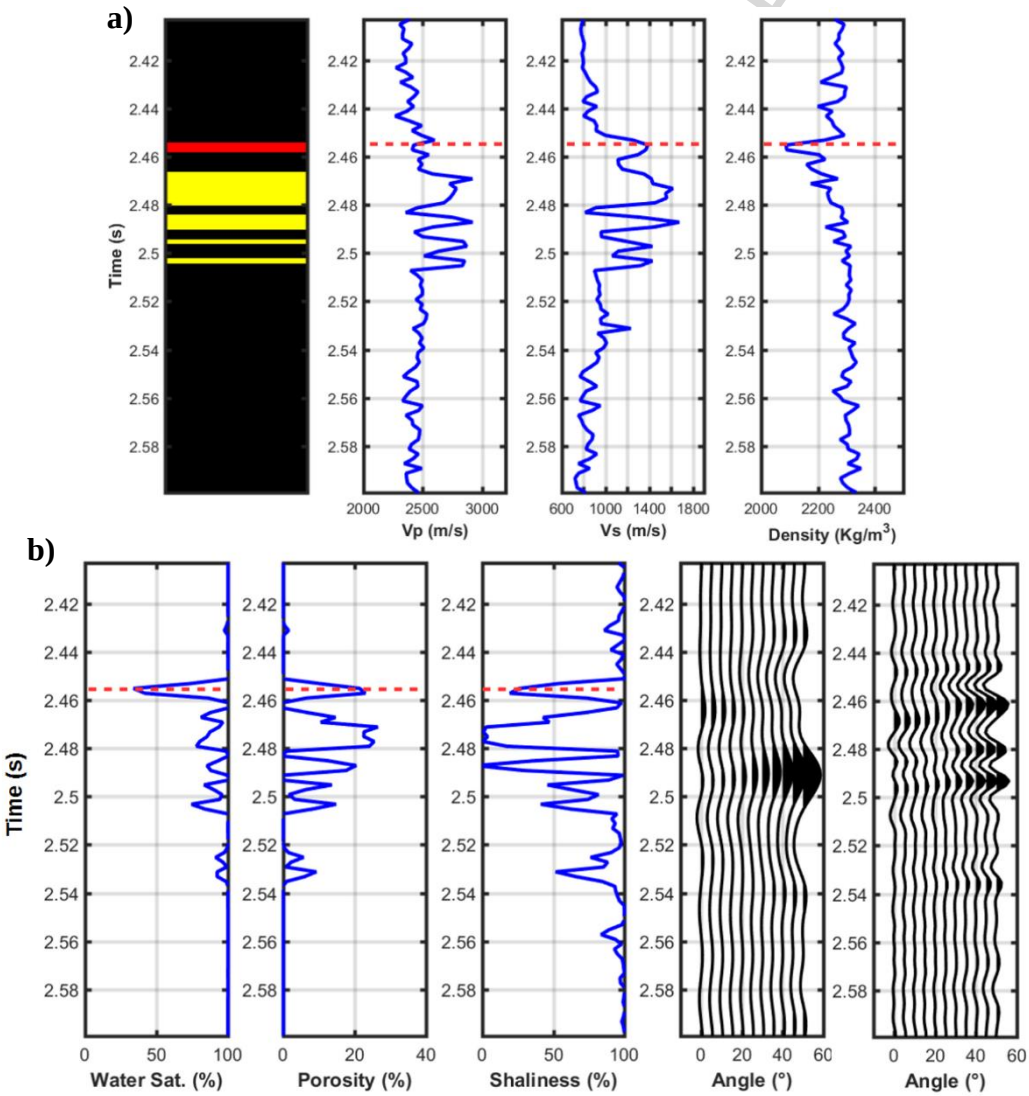


*Figure 6: Well log data (converted from depth to time using check-shot recordings) and two synthetic CMP gathers. a) From left to right are represented the litho-fluid facies classification (derived from the measured petrophysical properties), and the logged Vp, Vs and density values resampled at the seismic sampling interval. In the leftmost plot, black, yellow and red colors refer to shale, brine sand and gas sand, respectively. b) From left to right we represent the water saturation, porosity and shaliness values (derived from well log data and rescaled to the seismic*

*sampling interval) and two synthetic seismograms computed with a 20-Hz and 50-Hz Ricker wavelet, respectively. In a) and b) the dashed red lines identify the top of the reservoir that is a shale-gas sand interface.*

To validate our AVA-petrophysical inversion algorithm and to check the reliability and suitability of the derived rock-physics model used to rewrite the Zoeppritz equation, we perform an inversion of synthetic seismic data. The seismic data have been computed considering the *Vp, Vs* and density values (shown in Figure 6a) and using a 1D convolutional forward modelling based on the exact Zoeppritz equations, with a Ricker wavelet as the source signature. Figure 6b shows two different CMP gathers obtained with a 20-Hz and 50-Hz Ricker wavelet. In both cases we observe that the target sand generates a class III AVA anomaly (Castagna and Swan, 1997) and from their comparison it is also clear that this AVA anomaly, due to the very limited thickness of the gas-saturated layer, becomes more and more prominent as the frequency bandwidth of the seismic data increases. In particular, the decrease of the dominant frequency of the source signature produces an increase of the interference between adjacent reflections that tends to progressively mask the AVA anomaly. We investigate in more detail this issue and its effects on the estimated petrophysical properties in the final part of this section.

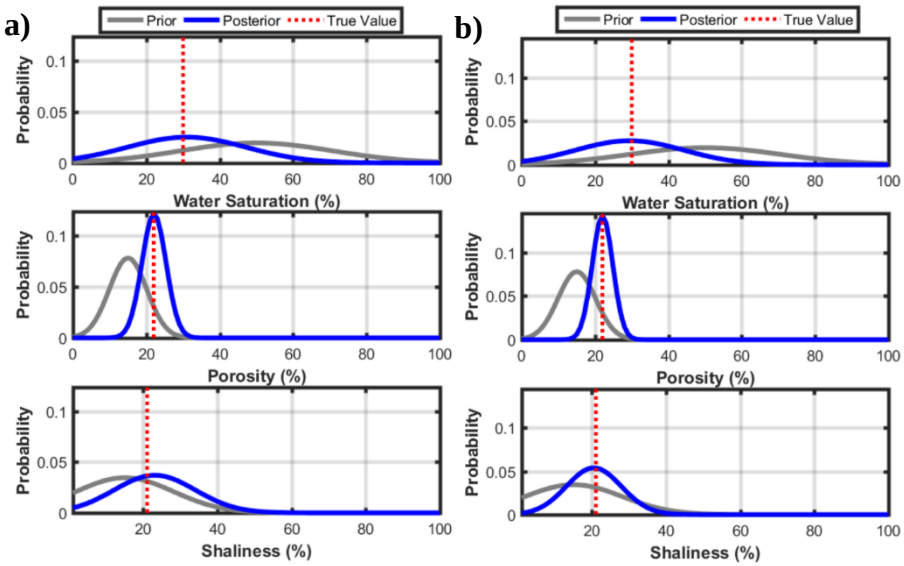


*Figure 7: a) And b) 1D marginal a-priori distributions (grey lines) derived from well log information and a-posteriori marginal PPDs, $p(m|Rpp_{obs})$ estimated by the AVA-petrophysical inversion (blue lines). a) Distributions for the narrow-angle inversion. b) Distributions for the wide-angle inversion. The vertical red dashed lines indicate the true values resulting from well log analysis.*

Figure 7 shows the a-priori and a-posteriori marginal distributions obtained applying our AVA-petrophysical inversion to the target reflection in case of a 50-Hz Ricker wavelet and imposing a signal to noise ratio equal to 10 in the synthetic seismogram. In Figure 7a are represented the results obtained with a narrow-angle (0-30 degrees) inversion, whereas Figure 7b illustrates the results for the wide-angle (0-60 degrees) inversion. The a-priori petrophysical distribution (defined by the a-priori mean values, $m_{prior,}$ and a-priori covariance matrix, $C_M$) has been obtained from actual well log recordings. Note that both the narrow- and wide-angle inversions yield posterior distributions centered at the true property values (see Figure 6b). However, the wide-angle inversion produces narrower posterior distributions for the shaliness and for the porosity compared with the narrow-angle inversion. The water saturation parameter is in both cases poorly resolved, thus confirming the conclusions drawn in the previous theoretical analyses. The fact that the AVA-petrophysical inversion yields final properties close to the true values confirms not only the applicability of the

method, but also the suitability of the derived rock-physics model for reservoir characterization in the investigated area.

To better investigate the influence of the seismic data resolution on the estimated petrophysical properties, we repeat the inversion on seismic data obtained by using source wavelets with different dominant frequencies. The results of this experiment for the inversion over an angle range of 0-60 degrees are shown in Figure 8. Note that in case of a low dominant frequency we tend to overestimate the water saturation and the shaliness and to underestimate the porosity. The estimated properties converge toward the actual properties ($Sh$ = 20%, $Sw$ = 30 % and $\varphi$= 22%) for a dominant frequency higher than 50-55 Hz. If consider a thickness of the reservoir sand layer equal to that encountered by the well, the reservoir properties are correctly estimated if the source wavelet has a dominant frequency higher than 50 Hz, approximately. Differently, in case of a lower dominant frequency we estimate only a low pass filtered version of the true petrophysical properties and such estimation is influenced by the petrophysical properties of shales or brine sands surrounding the target gas sand layer. This test demonstrates that in correspondence of the well location, due to the limited thickness of the reservoir layer and due to the very low resolution of the seismic data (characterized by a dominant frequency around 20 Hz), the AVA-petrophysical inversion will return an overestimation of the actual shaliness and water saturation values and an underestimation of the porosity.

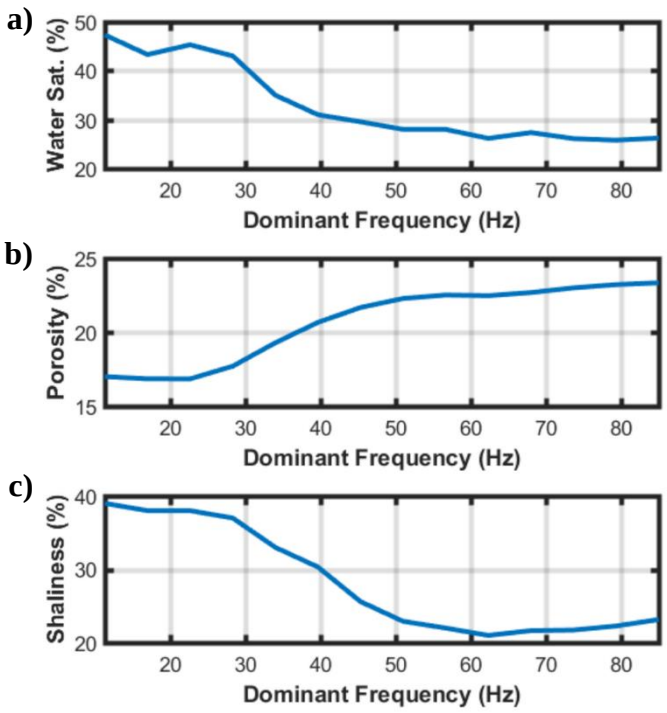


*Figure 8: The maximum a-posteriori (MAP) solution (that corresponds to the mean value of the Gaussian posterior probability distribution p(m|Rpp$_{obs}$)) versus the dominant frequency of the source wavelet used to compute the synthetic seismic data. a), b, And c) refer to water saturation, porosity and shaliness estimates, respectively.*

## 7 AVA-petrophysical inversion of field data

We test the described AVA-petrophysical inversion as part of appraisal studies of a productive gas-field located in offshore Nile Delta where seismic data were acquired with a maximum offset of 8 km and processed following a true-amplitude processing sequence. Borehole logs from 12 wells drilled in the field area provide seismic velocities, density and petrophysical information needed to compute the a-priori information ($C_M$ and $m_{prior}$ in equation 5b) and to derive the rock-physic model for the target zone.

Figure 9 represents a stack section extracted from the 3D seismic cube and a close-up around the target reflection, together with the interpreted top and base of the investigated channel system. The interpreted target reflection that will be considered in the following inversion is also represented. The well represented in Figure 9 is the same previously considered in the synthetic tests. Figure 10

shows the root mean square (RMS) amplitude map extracted from the stack volume along the target reflection. Note the high RMS amplitudes around the well position that are due to the significant contrasts in acoustic impedance at the reflecting interface that separates the overlying cap-rock and the underlying reservoir layer. The blue rectangle in Figure 10 encloses the area considered in the field data inversion.

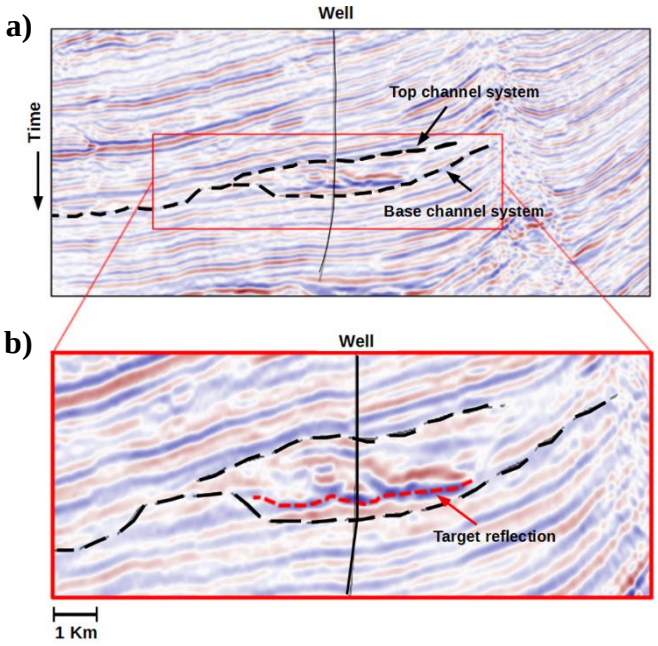


*Figure 9: a) Example of stack section extracted from the 3D seismic cube with indicated the top and base of the investigated channel system (black dashed lines). b) Close-up of the stack section in a) around the target reflection (red dashed line). In a) and b) the black continuous line is the trajectory of the well already considered in the synthetic inversion.*

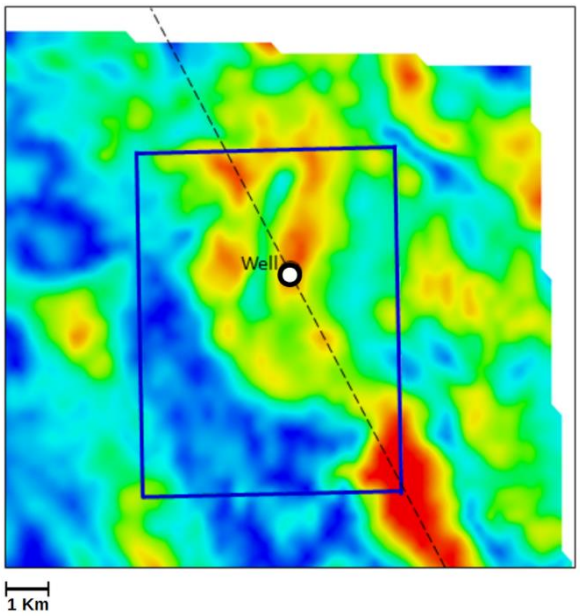


*Figure 10: Root mean square amplitude map computed along the target reflection and extracted from the stack volume. Blue and red colors code low and high RMS values, respectively. The dot represents the location of the well already considered in the synthetic inversion, whereas the black dashed line identifies the location of the stack section represented in Figure 9. The blue rectangle encloses the area considered in the field data inversion.*

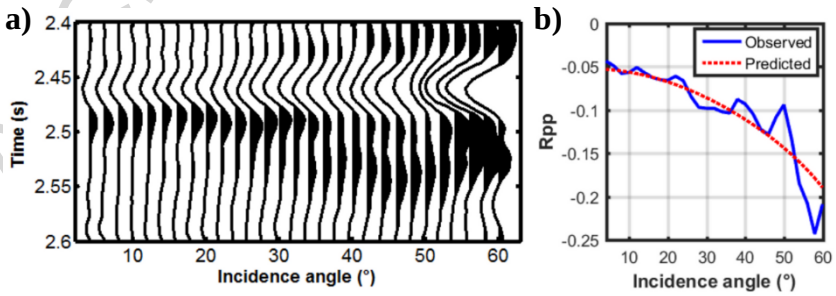


*Figure 11: a) Close-up of a time-migrated CMP gather around the target reflection. b) Observed (blue line) and predicted (red dotted line) P-wave reflection coefficients.*

We start our discussion about the petrophysical inversion of field data with a single inversion test performed on the CMP location that is the nearest to the well already considered in the synthetic AVA-petrophysical inversion (Figure 6a). Figure 11a shows a close-up of the considered CMP (with

offset converted to incidence angles) around the target reflections, whereas Figure 11b shows the extracted AVA, that is the P-wave reflection coefficients that constitute our observations ($Rpp_{obs}$). This AVA response has been extracted from the negative peak amplitude of the target reflection at 2.46 s, showed in Figure 11a, and normalized to the normal-incidence reflection coefficient derived from borehole logs. Note that in the selected CMP, the seismic data has an excellent S/N ratio over the whole angle range from 0 to 60 degrees. This characteristic makes it possible a clean extraction of the AVA response over a wide-angle range. Figure 11b also shows the best predicted *Rpp*, associated to the predicted petrophysical model. The PPDs of the petrophysical properties resulting from the wide-angle (0-60 degrees) inversion are shown in Figure 12a. The blue curves refer to the PPDs analytically derived, whereas the green curves refer to the PPDs numerically computed with the M-H algorithm. Note that porosity and, to a lesser extent, shale content are the best resolved parameters. For both these two parameters the maxima of the PPDs are shifted with respect to the position of the maxima of the a-priori distributions (grey curves), thus demonstrating that the solution is mainly driven by the observed AVA response. Conversely, the PPD of water saturation is quite broad and similar to the a-priori distribution, thus pointing out the limited sensitivity of AVA response to saturation even for a wide-angle range. With regard to the matching of the solutions (the maximum a-posteriori) with the actual values expected at the dominant frequency of the seismic data (see Figure 8), we note that all parameters are well recovered: porosity estimate is 17% with respect to 17%, the predicted shaliness is 36% with respect to 38% and the water saturation estimate is 42% with respect to 45%. To assess the resolution improvement that can be achieved by a wide-angle inversion, in Figure 12b we show the PPDs obtained by a narrow-angle (0-30 degrees) inversion. By comparing the PPDs resulting from the two inversions, we note that the wide-angle inversion produces a significant improvement in the estimation of shaliness and to a much less degree, in the water saturation estimate. Instead, the porosity is accurately estimated in both cases. In particular, note that the shaliness estimate moves toward the expected values of 38%, when passing from the narrow-angle to the wide-angle AVA inversion. In all the inversions, we observe a

good match between the green (numerical) and the blue (analytical) distributions. In particular, the curves obtained by the numerical approach show unimodal, nearly Gaussian, probability distributions. Note that the difference between the numerical distributions and the analytical ones increases as the incidence angle range is increased or, in other words, as the non-linearity of the inverse problem increases. However, despite this minor difference, the match between the blue and green curves validates the accuracy and the practical applicability of the approximated, analytical, uncertainty estimation.

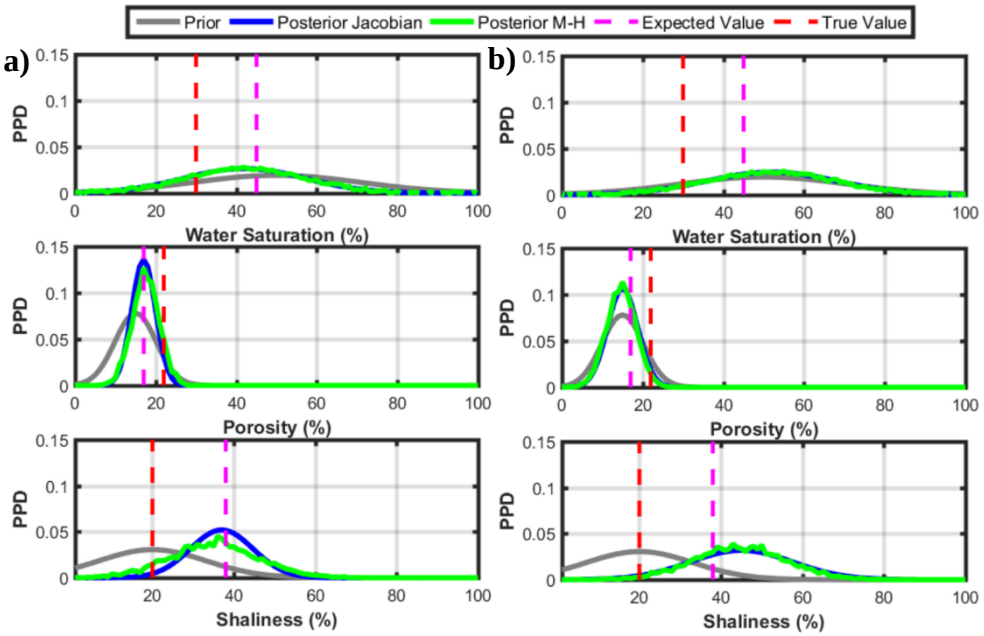


*Figure 12: a) And b) marginal a-priori distributions (grey lines) derived from well log information, marginal PPDs analytically derived (blue lines), and marginal PPDs computed with the Metropolis-Hastings algorithm (green lines). a) Distributions for the wide-angle inversion. b) Distributions for the narrow-angle inversion. The magenta dashed lines represent the expected estimated properties at the resolution of the available seismic data (see Figure 8), whereas the red lines are the true properties determined from well log data analysis.*

We now investigate the sensitivity of the inversion results (in terms of final PPDs) to variations in the assumed petrophysical cap-rock properties. To this end, we repeat the inversion for the CMP

gather previously considered (Figure 11) by fixing the properties of the cap-rock to different petrophysical values:

- *Sw*=100%, *Sh*=85%, $\varphi$= 5%;
- *Sw*=100%, *Sh*=92%, $\varphi$= 3%;
- *Sw*=100%, *Sh*=95%, $\varphi$= 1%.

In the three tests, we realistically assume a fully water-saturated cap-rock and only the shaliness and the porosity are varied. Figure 13 shows the final PPDs resulting from the three inversion tests. By comparing Figure 13 with the previous Figure 12, we note very minor variations in terms of MAP solutions. Figure 13 shows that the final PPD shifts along the horizontal axis if different petrophysical properties are assumed for the overlying cap-rock. However, from a practical point of view, this test demonstrates that reasonable variations of the petrophysical shale (cap-rock) properties can be neglected in the field data inversion. However, these variations can be considered an additional source of uncertainty and, if needed, they could be introduced into equation 5 to be accounted for in the inversion.

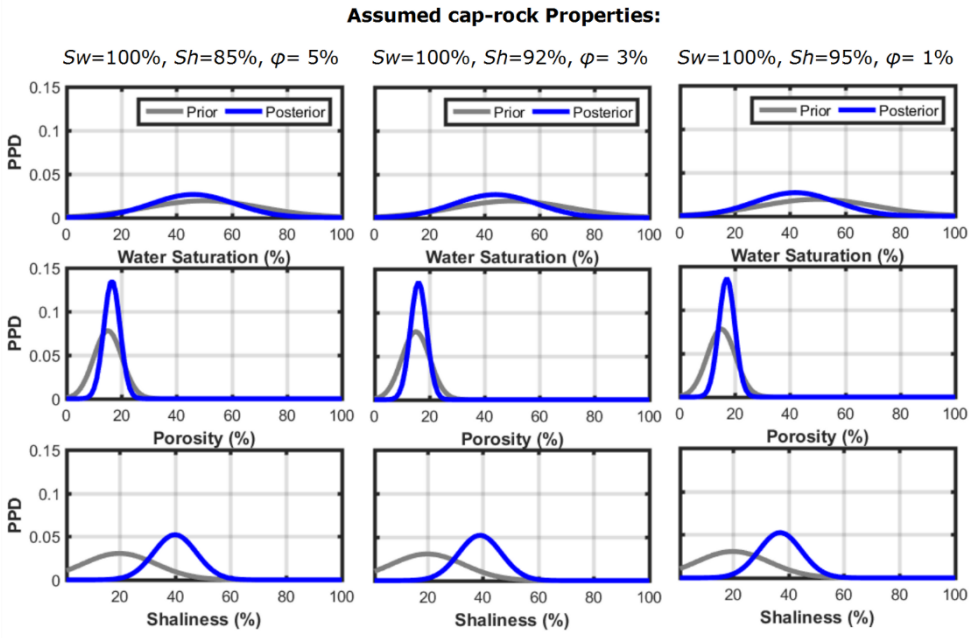


*Figure 13:From left to right: Final PPDs estimated for the CMP gather shown in Figure 11 if different cap-rock properties are assumed. See the text for additional comments.*

In Figure 14 we show the results of wide-angle AVA-petrophysical inversion performed in a different CMP location where well control is not available to validate the results. In Figure 14a we observe that the AVA response of the considered reflection is more similar to a class II AVA anomaly than to a class III anomaly. From the posterior marginal distributions shown in Figure 14b emerges that in this case, high water saturation and shaliness values and very low porosity characterize the investigated zone. These petrophysical properties can be associated to a sandy-shale layer rather than to a sand layer.

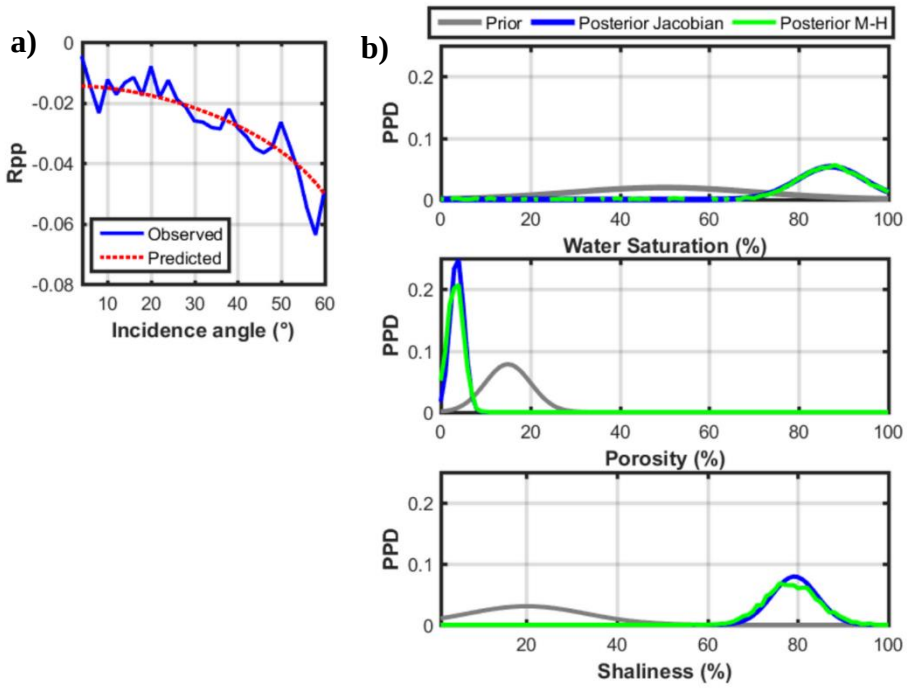


*Figure 14: a) Comparison between observed and predicted AVA responses for a CMP location in which the shale overlies a sandy-shale layer. b) Marginal a-priori distributions (grey lines) derived from well log information, marginal PPDs analytically derived by means of equation 4a (blue lines), and marginal PPDs computed with the Metropolis-Hastings algorithm (green lines). These distributions are obtained from a wide-angle AVA inversion.*

Finally, we show the results of the narrow- and wide-angle AVA-petrophysical inversions applied to a subset of CMPs extracted from the whole 3D volume and located inside the blue rectangle represented in Figure 10. We point out that no a-priori information about the spatial

correlation of petrophysical parameters has been used to constrain the inversion of adjacent CMPs. Therefore, the lateral continuity of our results is mainly related to the lateral correlation of seismic data that is dependent on the Fresnel zone and the corresponding migration operator. From the inversion of the 3D data, we can draw considerations that are in accordance with the previous analysis. More in detail, Figure 15a and Figure 16a show the MAP solution (the mean value of the posterior Gaussian distribution) estimated by our AVA-petrophysical inversion for the narrow-angle and wide-angle cases, respectively.

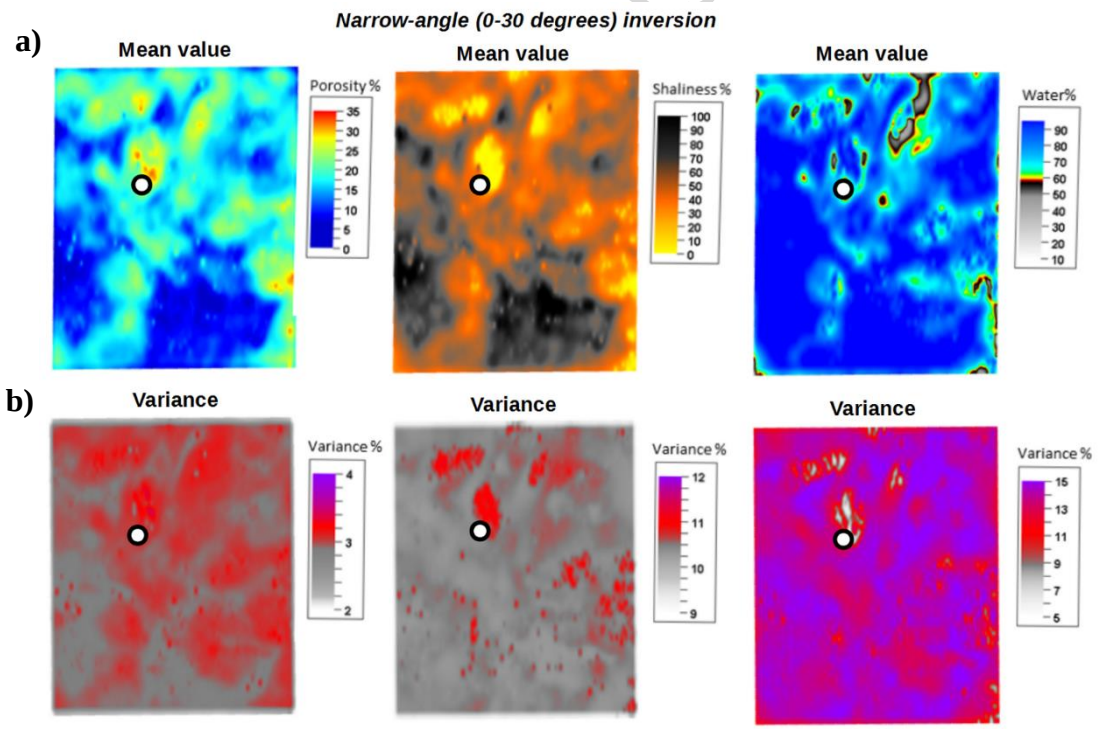


*Figure 15: a) MAP solution (that corresponds to the mean value of the Gaussian posterior distribution) resulting from the narrow-angle AVA-petrophysical inversion performed along the target reflection and within the area delimited by the blue rectangle of Figure 10. From left to right: porosity, shaliness and water saturation estimates, respectively. b) From left to right: variance values for porosity, shaliness and water saturation estimates, respectively. Note that the well (white dot) has intersected a sand channel characterized by high porosity and low water saturation and shaliness. Note that these maps do not refer to a single time-slice, but follow the interpreted top of the reservoir.*

These figures depict the lateral extension of the gas-saturated sand channel intersected by the well at 2.46 s, approximately. By comparing Figure 15a and Figure 16a, we note the fair similarity of the MAP estimates resulting from the two inversions. However, note that the sand channel intersected by the well, is better delineated on the MAPs resulting from the wide-angle inversion.

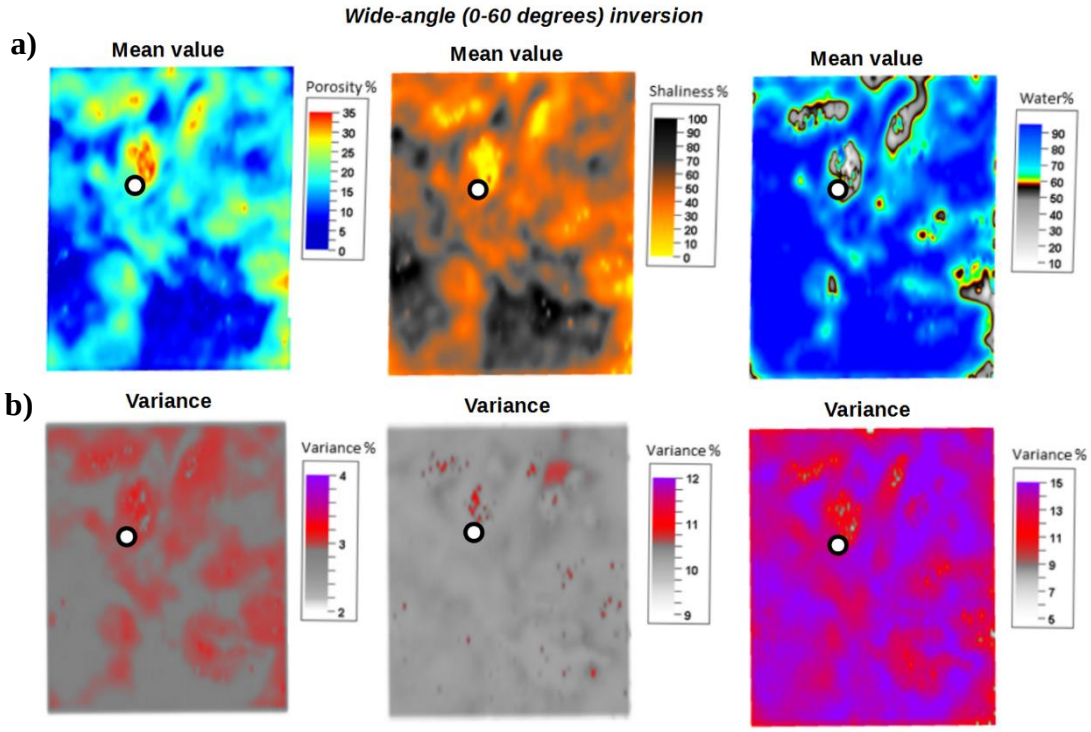


*Figure 16: a) MAP solution (that corresponds to the mean value of the Gaussian posterior distribution) resulting from the wide-angle AVA-petrophysical inversion performed along the target reflection and within the area delimited by the blue rectangle of Figure 10. From left to right: porosity, shaliness and water saturation estimates, respectively. b) From left to right: variance values for the porosity, shaliness and water saturation estimates, respectively. Note that the well (white dot) has intersected a sand channel characterized by high porosity value and low water saturation and shaliness values. By comparing with Figure 15, note the significant decrease of the uncertainty for the shaliness and the porosity estimates.*

The comparison of Figure 15b and Figure 16b makes clear the different variance values estimated by the two inversions. In particular, note the decreased uncertainty for the porosity, but particularly,

for the shaliness estimates when passing from the narrow-angle to the wide-angle inversion. Differently the uncertainty remains more or less constant for the water saturation.

## 8 Conclusions

We presented a reliable and computationally fast AVA-petrophysical inversion that directly estimates petrophysical properties and their associated uncertainties from observed P-wave AVA data. The inversion tests on the Nile Delta 3D seismic data confirmed the applicability of the method for the estimation of petrophysical properties and of their variations along the top of the considered reservoir. The estimated properties were consistent with borehole data and with the expected estimates at the resolution of the available seismic data. The method we propose makes use of the exact Zoeppritz equations re-parameterized in terms of the petrophysical properties of interest by means of an empirical multi-linear rock-physics model, properly calibrated for the area under investigation. Differently from using the classical narrow-angle approximation, this allows us to gain advantage of the long-offset/wide-angle seismic reflections that turn out to be quite effective in better constraining the shaliness estimates. For the analyzed case, the porosity resulted to be the best resolved parameter and it is well estimated with both the narrow-angle and the wide-angle AVA inversions, whereas the water saturation value is poorly resolvable in both cases. The close similarity between the analytical posterior probability distributions provided by a local linearization, and those numerically derived with a MCMC algorithm, demonstrated the practical applicability of the linear approximation for a reliable uncertainty quantification. From one hand, the pro of our algorithm is its very limited computational time. For example, the field data inversion required few minutes to run on an Intel i5@3.20 Hz. From the other hand, our method is limited by its strictly target-oriented approach that requires a previous accurate interpretation that individuates the target reflections in the investigated area.

**Acknowledgements**

The authors wish to thank EDISON for making the seismic and the well log data available and for the permission to publish this work. The analysis and visualization of the seismic data at the University of Pisa was performed by means of the Promax 3D Software of Landmark Graphics Corporation, who is gratefully acknowledged.

**References**


1. Aki, K., and Richards,P. G. (1980). Quantitative seismology: W. H. Freeman & Co.
2. Aleardi, M., and Mazzotti, A. (2014). A feasibility study on the expected seismic AVA signatures of deep fractured geothermal reservoirs in an intrusive basement. Journal of Geophysics and Engineering, 11(6), 065008. Doi: 10.1088/1742-2132/11/6/065008
3. Aleardi, M. (2015). The importance of the Vp/Vs ratio in determining the error propagation, the stability and the resolution of linear AVA inversion: a theoretical demonstration. Bollettino di Geofisica Teorica ed Applicata, 56(3), 357-366. Doi: 10.4430/bgta0156
4. Aleardi, M., Mazzotti, A., Tognarelli, A., Ciuffi, S., and Casini, M. (2015). Seismic and well log characterization of fractures for geothermal exploration in hard rocks. Geophysical Journal International, 203(1), 270-283. Doi: 10.1093/gji/ggv286
5. Aleardi M., and Tognarelli A., (2016). The limits of narrow and wide-angle AVA inversions for high Vp/Vs ratios: An application to elastic seabed characterization. Journal of Applied Geophysics, 161, 54-68. Doi: 10.1016/j.jappgeo.2016.05.009
6. Aleardi, M., and Mazzotti, A. (2017). 1D elastic FWI and uncertainty estimation by means of a hybrid genetic algorithm-gibbs sampler approach. Geophysical Prospecting, 65, 64-85. Doi: 10.1111/1365-2478.12397.
7. Aleardi, M., and Ciabarri F., (2017). Assessment of different approaches to rock-physics modeling: A case study from offshore Nile Delta. Geophysics, 82(1), MR15-MR25. Doi: 10.1190/geo2016-0194.1
8. Aleardi, M., Ciabarri, F., Gukov, T., Giussani, M., and Mazzotti, A. (2017). A single-step Bayesian petrophysical inversion algorithm based on a petrophysical reformulation of the P-wave reflection coefficients. In 79th EAGE Conference and Exhibition, Paris, France. Doi: 10.3997/2214-4609.201700902
9. Avseth, P., Mukerji, T., and Mavko, G. (2005). Quantitative seismic interpretation: Applying rock physics tools to reduce interpretation risk. Cambridge University Press.

10. Bosch, M. (2004). The optimization approach to lithological tomography:Combining seismic data and petrophysics for porosity prediction. Geophysics, 69, 1272–1282. Doi: 10.1190/1.1801944

11. Bosch, M., Cara, L., Rodrigues, J., Navarro, A., and Díaz, M. (2007). A Monte Carlo approach to the joint estimation of reservoir and elastic parameters from seismic amplitudes. Geophysics, 72(6), O29-O39. Doi: 10.1190/1.2783766

12. Bosch, M., Bertorelli, G., Álvarez, G., Moreno, A., and Colmenares, R. (2015). Reservoir uncertainty description via petrophysical inversion of seismic data. The Leading Edge, 34(9), 1018-1026. Doi: 10.1190/tle34091018.1

13. Castagna, J. P., and Swan, H. W. (1997). Principles of AVO crossplotting. The leading edge, 16(4), 337-344. Doi: 10.1190/1.1437626

14. Chiappa, F., and Mazzotti, A. (2009). Estimation of petrophysical parameters by linearized inversion of angle domain pre-stack data. Geophysical Prospecting, 57, 413-426. Doi: 10.1111/j.1365-2478.2008.00742.x

15. Contreras, A., Torres-Verdin, C., Chesters, W., Kvien, K., and Fasnacht, T. (2005). Joint stochastic inversion of petrophysical logs and 3D pre-stack seismic data to assess the spatial continuity of fluid units away from wells: Application to a Gulf-of-Mexico deepwater hydrocarbon reservoir. Transactions of the 46th Annual Logging Symposium, Society of Petrophysicists and Well Log Analysts, 1–15.

16. De Nicolao A., Drufuca G. and Rocca F. (1993). Eigenvalues and eigenvectors of linearized elastic inversion. Geophysics, 58, 670-679. Doi: 10.1190/1.1443451

17. Draper, N.R., and Smith, H. (1985). Applied Regression Analysis. 2nd ed. JohnWiley & Sons Inc.

18. Drufuca, G., and Mazzotti, A. (1995). Ambiguities in AVO inversion of reflections from a gas-sand. Geophysics, 60(1), 134-141. Doi: 10.1190/1.1443740

19. Gelman, A., Carlin, J. B., Stern, H. S., Dunson, D. B., Vehtari, A., and Rubin, D. B. (2013).

Bayesian data analysis. CRC press.

20. Gouveia, W. P., and Scales, J. A. (1998). Bayesian seismic waveform inversion: Parameter estimation and uncertainty analysis. Journal of Geophysical Research: Solid Earth, 103(B2), 2759-2779. Doi: 10.1029/97JB02933
21. Grana, D., and Della Rossa, E. (2010). Probabilistic petrophysical-properties estimation integrating statistical rock physics with seismic inversion. Geophysics, 75(3), O21-O37. Doi: 10.1190/1.3386676
22. Grion S., Mazzotti A and Spagnolini U. (1998). Joint estimation of AVO and kinematic parameters. Geophysical Prospecting, 46, 405-422. Doi: 10.1046/j.1365-2478.1998.970332.x
23. Hastings, W. K. (1970). Monte Carlo sampling methods using Markov chains and their applications. Biometrika, 57(1), 97-109.
24. Li, D., and Zhang, F. (2015). Direct Estimation of Petrophysical Properties Based on AVO Inversion. In 2015 SEG Annual Meeting. Society of Exploration Geophysicists, 2886-2890. Doi: 10.1190/segam2015-5840282.1
25. Mazzotti A. (1990). Prestack amplitude analysis methodology and application to seismic bright spots in the Po Valley, Italy. Geophysics, 55, 157-166. Doi: 10.1190/1.1442822
26. Mazzotti A. (1991). Amplitude, Phase and Frequency versus Offset Applications. Geophysical Prospecting. 39, 863-886. Doi: 10.1111/j.1365-2478.1991.tb00348.x
27. Mazzotti, A., and Zamboni, E. (2003). Petrophysical inversion of AVA data. Geophysical Prospecting, 51, 517-530. Doi: 10.1046/j.1365-2478.2003.00389.x
28. Mavko, G., Mukerji, T., and Dvorkin, J. (2009). The rock physics handbook: Tools for seismic analysis of porous media. Cambridge university press.
29. Mukerji, T., Jørstad, A., Avseth, P., Mavko, G., and Granli, J. R. (2001). Mapping lithofacies and pore-fluid probabilities in a North Sea reservoir: Seismic inversions and statistical rock physics. Geophysics, 66(4), 988-1001. Doi: 10.1190/1.1487078

30. Ostrander W. (1984). Plane-wave reflection coefficients for gas sands at non-normal angles of incidence. Geophysics, 49(10), 1637-1648. Doi: 10.1190/1.1441571

31. Riedel, M., and Theilen, F. (2001). AVO investigations of shallow marine sediments. Geophysical Prospecting, 49(2), 198-212. Doi: 10.1046/j.1365-2478.2001.00246.x

32. Riedel, M., Dosso, S. E., and Beran, L. (2003). Uncertainty estimation for amplitude variation with offset (AVO) inversion. Geophysics, 68(5), 1485-1496. Doi: 10.1190/1.1620621

33. Rutherford, S. R., and Williams, R. H. (1989). Amplitude-versus-offset variations in gas sands. Geophysics, 54(6), 680-688. Doi: 10.1190/1.1442696

34. Sajeva, A., Aleardi, M. and Mazzotti, A. (2016) Combining Genetic Algorithms, Gibbs Sampler, and Gradient-based Inversion to Estimate Uncertainty in 2D FWI. 78th EAGE Conference and Exhibition, Vienna, Austria. doi: 10.3997/2214-4609.201601543.

35. Sambridge, M. (1999). Geophysical inversion with a neighbourhood algorithm—II. Appraising the ensemble. Geophysical Journal International, 138(3), 727-746. Doi: 10.1046/j.1365-246x.1999.00900.x

36. Sambridge, M., and Mosegaard, K. (2002). Monte Carlo methods in geophysical inverse problems. Reviews of Geophysics, 40(3), 3-1. Doi: 10.1029/2000RG000089

37. Sen, M. K., and Stoffa, P. L. (1996). Bayesian inference, Gibbs' sampler and uncertainty estimation in geophysical inversion. Geophysical Prospecting, 44(2), 313-350. Doi: 10.1111/j.1365-2478.1996.tb00152.x

38. Skopintseva, L., and Alkhalifah, T. (2013). An analysis of AVO inversion for postcritical offsets in HTI media. Geophysics, 78(3), N11-N20. Doi: 10.1190/geo2011-0288.1

39. Tarantola, A. (2005). Inverse problem theory and methods for model parameter estimation. siam.

40. Zhu, X., and McMechan, G.A. (2012). Elastic inversion of near-and postcritical reflections using phase variation with angle. Geophysics, 77(4), R149-R159. Doi: 10.1190/geo2011-

0230.1

41. Zunino, A., Mosegaard, K., Lange, K., Melnikova, Y., and Mejer Hansen, T. (2014). Monte Carlo reservoir analysis combining seismic reflection data and informed priors. Geophysics, 80(1), R31-R41. Doi: 10.1190/geo2014-0052.1

**Appendix A**

To compute the matrix $C_{Rppobs}$ of equation 5 we assume a normally distributed noise with a null mean value and a diagonal covariance matrix. In particular, the $C_{Rppobs}$ matrix is computed by comparing the AVA responses of adjacent CMP gathers, and by assuming that these responses are produced by similar petrophysical properties. Then, the differences between the AVA responses extracted from adjacent CMPs have been attributed only to noise contamination.

The differences between the logged elastic properties and the elastic properties predicted by the empirical RPM, are used to derive the $C_{RPM}$ matrix (see equation 5) with an approach similar to that described in Gouveia and Scales (1998). In particular, we assume that this difference follows a Gaussian probability distribution with a given covariance matrix and a null mean value. This probability distribution (Figure 17) describing the uncertainties associated to the RPM, can be written as:

$$p(\varepsilon) = N(m; \mu_\varepsilon = 0, \Sigma_\varepsilon) \qquad (A1)$$

where $N$ represents the normal distribution with a mean value $\mu_\varepsilon$ and a covariance matrix $\Sigma_\varepsilon$. The steps used to derive the $C_{RPM}$ matrix are the following:

1. Consider a single reflecting interface separating an overlying shale to an underlying sand;
2. Impose for the shale porosity and gas saturation values equal to 0% and a shaliness of 100%;
3. Define the petrophysical sand properties by drawing random values from the a-priori distribution of the petrophysical properties $p(m)$;
4. Apply the RPM to derive the elastic properties for the upper and lower medium;
5. Perturb the elastic properties for the sand (derived at step 4) by adding random vector drawn from the distribution $p(\varepsilon)$;
6. Derive the AVA response for the reflecting interface using the exact Zoeppritz equations;

7. Repeat steps from 5) to 7) $q$ times and collect all the $q$ AVA responses, each one generated by a perturbation of the elastic properties of the sand layer.

The differences between the $q$ simulated AVA responses, quantify the fluctuations due to uncertainties in the rock-physics model, and are used to estimate the covariance matrix $C_{RPM}$ of equation 6.

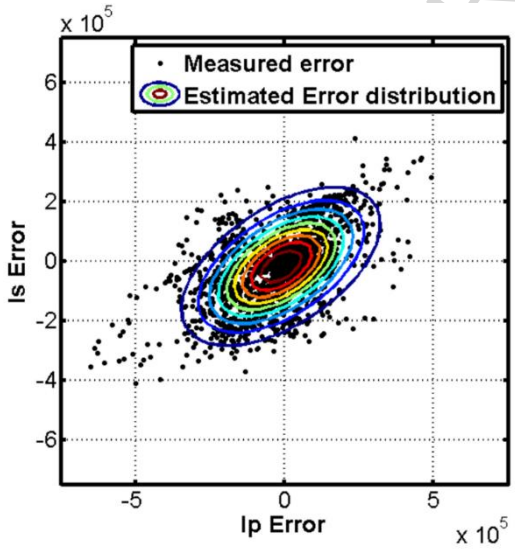


*Figure 17: Error distributions p(ε) associated to the empirical RPM projected onto the Ip-Is plane. The black dots show the difference between actual and predicted Ip and Is values, whereas the colored contours represent the Gaussian distribution derived on the ensemble of black dots, that describe the uncertainties in the RPM definition (red and blue colors code high and low probability, respectively). Note the positive correlation between the Ip and Is errors and that the Gaussian distribution has a mean value very close to the assumed value of zero.*

Figure 18 shows an example of the final $C_D$ matrix obtained by summing the $C_{Rppobs}$ and $C_{RPM}$ matrices. Note that due to the difficulty related to the extraction of AVA responses at high incidence angles, the diagonal terms of the $C_{Rppobs}$ matrix increases as the incidence angle increases. These difficulties can be associated to interference effects that become more and more significant as the incidence angle increases. In addition, the increasing values of the terms in the $C_{RPM}$ matrix as the incidence angle increases, proves that the uncertainties in the rock-physics model generate AVA

responses with differences that increase as the angle increases. These two characteristics produce a matrix $C_D$ that gives less weight to the data observed at high incidence angles respect to those observed at low angles.

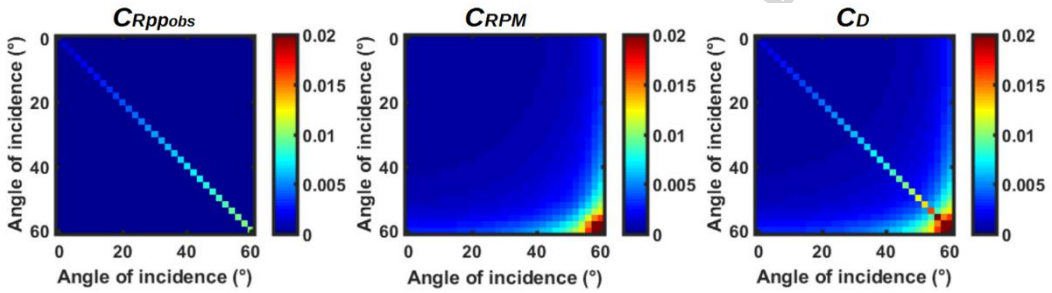


*Figure 18: An example showing the matrix $C_D$ obtained by summing the matrices $C_{Rppobs}$ and $C_{RPM}$.*

## Highlights

Implementing a fast, probabilistic AVA-petrophysical inversion

Rewriting the Zoeppritz equations in terms of petrophysical properties

Studying the influence of wide-angle reflections in AVA-petrophysical inversion